

Dust Scattering in Miras R Car and RR Sco resolved by optical interferometric polarimetry

M.J. Ireland, P.G. Tuthill, J. Davis, W. Tango

School of Physics, University of Sydney NSW 2006, Australia

23 November 2018

ABSTRACT

We present optical interferometric polarimetry measurements of the Mira-like variables R Car and RR Sco, using the Sydney University Stellar Interferometer. By making visibility measurements in two perpendicular polarisations, the relatively low-surface brightness light scattered by atmospheric dust could be spatially separated from the bright Mira photospheric flux. This is the first reported successful use of long-baseline optical interferometric polarimetry. Observations were able to place constraints on the distribution of circumstellar material in R Car and RR Sco. The inner radius of dust formation for both stars was found to be less than 3 stellar radii: much closer than the expected innermost stable location for commonly-assumed astrophysical “dirty silicate” dust in these systems (silicate dust with a significant iron content). A model with the dust distributed over a shell which is geometrically thin compared to the stellar radius was preferred over an outflow. We propose dust components whose chemistry and opacity properties enable survival at these extreme inner radii.

Key words: techniques: interferometric – stars: variables: Miras – stars: AGB and post-AGB

1 INTRODUCTION

The processes of dust formation and mass loss in evolved giants and supergiants remains poorly understood despite its manifold and profound implications to the cycle of matter through stars and back into the ISM. An extensive observational and phenomenological literature (see e.g. Habing (1996) for a review) bears witness to the barrage of astrophysical techniques applied to this problem, and progress has been considerable in many important areas. However, fundamental uncertainties remain over the mechanisms of elevation of material, chemical nucleation of the dust, and subsequent outflow and global properties of the wind. As an example of the gap in our understanding, there has been to date no self-consistent physical model of the atmosphere of an evolved O-rich giant which encompasses the upper regions including even the most important basic phenomena: non-grey radiative transfer, pulsation, shocks, convection, non-equilibrium dust formation and the molecular atmosphere.

From an observational perspective, progress has been hampered until now by the difficulties inherent in imaging material on size scales of a few AU which encompass the photospheres themselves and the dust formation and acceleration regions. Although modern long-baseline optical/IR interferometry is capable of accessing these scales, imaging is not straightforward as targets can be complex, deeply embedded and often asymmetric. In particular for many Mira-type variables, the relatively low surface-brightness material in the outflow can be very difficult to detect against the high luminosity stellar flux.

The stellar photosphere and circumstellar dust shell are usu-

ally treated as completely separate regimes, as justified by the following simple argument. As a first approximation, one might consider that dust grains in an optically thin envelope are grey or nearly so, and exist in thermal equilibrium with the radiation field. Furthermore, we can approximate the star as having a small angular extent, so that the mean intensity, $J(\lambda)$ at the dust condensation radius R_c is equal to the luminosity of the central star $L(\lambda)$ divided by $16\pi^2 R_c^2$. In this case Equation 1 gives an estimate of the dust formation radius (here R_s the radius of the central star, T_s the effective temperature of the star and T_c the dust condensation temperature). Given an effective temperature of 3000 K and a dust condensation temperature of 1100 K, the dust formation radius is 3.7 stellar radii, which means that the physics of the photosphere and the circumstellar environment could be considered well-separated. Where dust is considered to be non-grey, but the dust formation radius still lies well-outside the photosphere, conservation of energy and radiative equilibrium gives Equation 2, where Q is the absorption coefficient of the dust and B is the Planck function in the form which gives power per unit area per steradian per unit wavelength. Further discussion of these kinds of approximations can be found in Schutte & Tielens (1989).

$$R_c = \frac{R_s}{2} \left(\frac{T_s}{T_c} \right)^2 \quad (1)$$

$$R_c = \sqrt{\frac{\int Q_{\text{abs}}(\lambda) L(\lambda) d\lambda}{16\pi^2 \int Q_{\text{abs}}(\lambda) B(\lambda, T_c) d\lambda}} \quad (2)$$

The absorption coefficients for dust around O-rich Mira are often assumed to be those of “dirty” silicates (Jones & Merrill

1976; Ossenkopf et al. 1992). These silicates have optical constants very similar to amorphous olivine $Mg_xFe_{1-x}SiO_4$ with $x = 0.5$ (Dorschner et al. 1995), with the exception of the spectral range $2-8\ \mu m$, where inclusions such as solid Fe are required to match observationally derived optical constants. Olivine with $x = 0.5$ can form only slightly closer to the star than grey dust. Using the emitted flux from a 3000 K effective temperature Mira model from Ireland et al. (2004a) (the M09n model), the optical constants from Dorschner et al. (1995) and an assumed condensation temperature of 1100 K, this olivine can form at a radius of 6.4 stellar radii: still a comfortable distance from the upper atmosphere of the star.

Apart from the optical properties, the other factor governing grain survival at smaller radii is the sublimation temperature. The dust species often considered to be the first to form in higher effective temperature stars from semi-empirical considerations is corundum (Egan & Sloan 2001), Al_2O_3 , which is stable at considerably higher temperatures than silicates (Salpeter 1977). Its formation radius for this same 3000 K model star is 2.1 stellar radii, using the optical constants from Koike et al. (1995) and an assumed condensation temperature of 1400 K.

The multi-wavelength diameter measurements of six Mira-like variables made by Ireland et al. (2004b) show an increase in apparent diameter from 900 nm to 700 nm with a component which appears uncorrelated with the strength of TiO bands. These observations are best explained by scattering from dust closer than a few stellar radii (although molecular line blanketing makes quantitative interpretation difficult). The presence of extensive dust this close is, as discussed above, difficult to reconcile with the conventional wisdom on dust formation around AGB stars.

Despite the fact that the net polarisation arising from a spherically symmetric dust shell is zero, it is possible to separate it from the unpolarised photosphere with a polarisation-sensitive high-resolution measurement. Scattering from the dust shell will have a polarisation at any point with the E field in an azimuthal direction with respect to the stellar centre. This is due to the simple relationship that scattered light from small particles in the Rayleigh limit is polarised orthogonal to the plane containing the source, scatterer and observer.

If we now consider the response of a long-baseline interferometer which measures the Fourier components (called visibilities when total flux is normalised to unity) of such an image, these will have different amplitudes and phases in different polarisations. For a partially-resolved circularly symmetric source, the linear polarisation with the E field parallel to the baseline of observation will have a lower amplitude and the same phase as the visibility measured using the polarisation perpendicular to the baseline. An attempt was made using this technique to detect scattering by free electrons around β Orionis using the long-baseline Narrabri Stellar Intensity Interferometer (Brown et al. 1974), but the instrument lacked the required sensitivity. Here we report the first successful use of this technique on a long-baseline optical interferometer. The observational technique is described in the following section, while Section 3 gives the results and Section 4 a discussion and astrophysical interpretation.

2 OBSERVATIONS

The Sydney University Stellar Interferometer (SUSI) is a long baseline optical interferometer with presently operational baselines from 5 to 160 m (further details can be found in Davis et al. (1999)). The observations presented here used 5 and 10 m baselines and

a filter with central wavelength of 900 nm and full-width half-maximum 80 nm. This filter was chosen so as to minimise contamination from the strongest features caused by the TiO molecule. It is in principle possible to measure visibilities at arbitrary polarisations through the use of quarter-wave plates and polarisers at arbitrary orientations. For a discussion of a general way to calibrate a long baseline interferometer for imaging in all Stokes parameters, see Elias (2004). Due to polarisation-dependent phase-shifts and mirror reflectivities over the many mirrors in the SUSI optical chain, arbitrary initial polarisation states are not well preserved. The measurements therefore are restricted to states with pure vertical and horizontal electric field orientation with respect to the optical path. While they will be attenuated, these states should not suffer mixing from any reflection with the exception of the initial reflection off the siderostat when observing away from the meridian. Care was taken to only observe stellar targets when near the meridian. Given SUSI's North-South baseline orientation, this observing strategy resulted in visibility measurements with the E field at all times being within 19 degrees of perpendicular (V_{\perp}) or parallel (V_{\parallel}) to the baseline. For crucial observations where a direct comparison was made between the visibilities in these two polarisations, data were restricted further to lie within 8 degrees of these orientations.

The beam combining system used for these observations consisted of a pupil-plane beam combiner feeding two Avalanche Photo-Diode (APD) detectors. By repeatedly scanning the optical delay linearly through the white-light fringe position, the light detected from each output of the combining beamsplitter is modulated at a frequency that depends on the scanning rate and the observing wavelength, with the fringe signals 180 degrees out of phase at the two outputs. A description of a similar system can be found in Baldwin et al. (1994), and further details of the beam combining system used for these observations will be found in Davis et al. (2005) (in preparation). Although the two outputs are usually used differentially to reduce the effects of scintillation noise, it is possible to obtain an estimate for the fringe visibility from only one output, as in Figure 1. The use of only one detector means that the bias in the power spectrum is not flat due to scintillation, and incorrect subtraction of this bias becomes an additional error source for low V^2 . The observational strategy employed consisted of two separate parts: the first aimed at measuring V_{\perp} and V_{\parallel} separately, while the second measured the ratio V_{\perp}/V_{\parallel} . These are described in turn below.

Firstly, polarisers were co-aligned and placed in front of the two outputs of the beam combiner, enabling a high signal-to-noise measurement of the correlation in linear polarised light. As is usual with optical interferometry measurements, observations of targets were interleaved with un- or partially-resolved reference stars to calibrate the system correlation (the V^2 response to a point source) as a function of time. Before use in adjusting the science measurements, this system response was also corrected for the known nonzero diameters of the reference stars given in Table 1. In this phase of the observational program, measurements were predominantly made of V_{\perp} which had a much higher signal-to-noise than V_{\parallel} . This is mainly due to partially polarising beamsplitters used at SUSI to split off light to the tip/tilt adaptive optics camera, which had the effect of significantly lowering the system throughput for V_{\parallel} .

The second part of the observing strategy consisted of simultaneous observations of V_{\perp} and V_{\parallel} , made possible by placing polarisers with orthogonal orientations in front of the two outputs of the beam combiner. These observations gave a measurement of the

Table 1. Assumed diameters for the calibrator stars used for these observations

Star	Uniform Disk (UD) Diameter (mas)	Method ²
HR 6241	5.9	VB99
HR 6630	4.2	VB99
HR 4050	4.9	C99
HR 6553	2.2 ¹	O82
HR 3685	1.54	O82
HR 3884	2.5,2.8	S05

¹ This star also has a companion 3.39 magnitudes fainter and at distance of 6.47'' (figures taken from the *HIPPARCOS* catalogue). This was over-resolved by SUSI and taken into account in the calibrated values for V^2 .

² VB99: Diameters estimated from the B-K relationship from van Belle (1999), using the photometry from the catalogue of Ducati (2002).

C99: Diameter taken from Cohen et al. (1999), with limb-darkening correction from Claret (2000).

O82: Diameters taken from Ochsenbein & Halbwachs (1982).

S05: Diameters of this Cepheid taken from near-simultaneous measurements at SUSI, at early April and early May epochs, consistent with the published diameters of Kervella et al. (2004).

ratio V_\perp/V_\parallel , and due to the simultaneous data, the ratio could be obtained independent of seeing effects so that rapidly interspersing calibrator star observations was no longer necessary, and longer total integration times were possible. Calibrator stars, observed at a different time of night, were still used for these observations to correct for instrumental effects that might affect this visibility ratio. Some calibrators were moderately resolved, and calibrators of a range of spectral types were used, however there was no evidence for systematic variation of the visibility ratio V_\perp/V_\parallel between calibrator stars.

A typical observation in a single polarisation consisted of 4000 50 ms sweeps through the fringe envelope, while the simultaneous observations of V_\perp and V_\parallel contained up to 20000 50 ms sweeps through the fringe envelope. The slew and acquisition time between source and calibrator generally averaged 3-4 minutes. Details of all observations can be found in Table 2. Note that squared visibility (or correlation) quantities are listed, because in the photon-noise limited regime, squared visibility must be averaged over many scans and error distributions are closest to Gaussian in these quantities.

There are several sources of systematic error in the measurement of V_\parallel^2/V_\perp^2 . One error source which was corrected for in the values in Table 2 was a 5 nm shift in effective centre wavelength between the filter in each output channel. The effect of this was to make the source appear slightly more resolved in one channel than the other. This effect was well characterised by observing in a mode where both output channels observed the same polarisation state, and resulted in a maximum correction of 3% in V_\parallel^2/V_\perp^2 for the most well-resolved observation.

Other errors, not included as their effects were computed to be small, consisted of imperfect polariser alignment, offsets between the actual polarisation passed and the ideal desired sky orientation, and depolarisation and mixing due to alignment errors in the beam train. With the assumptions of spherical symmetry and Rayleigh scattering, each of these effects multiplies $V_\parallel - V_\perp$ by a factor γ which has a modulus smaller than 1. We will define ϕ to be the azimuthal coordinate describing the rotation of the siderostat normal about a horizontal north-south axis, with $\phi = 0$ describing the meridian. The effect of vertical/horizontal linear polarisation

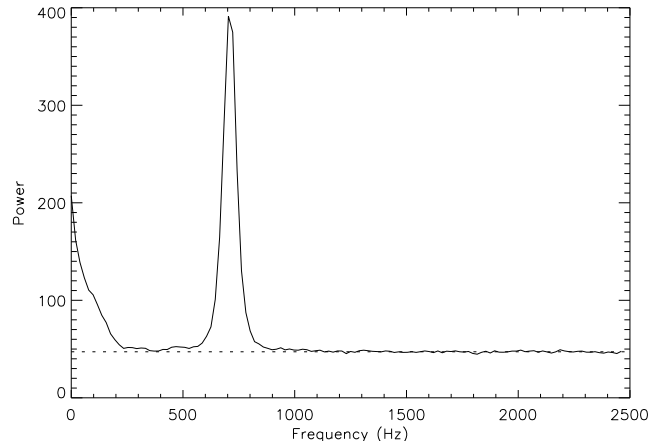


Figure 1. An example power spectrum (for the calibrator star HR 6241 in the 900 nm filter) obtained from averaging the power spectra from 3000 fringe scans together. Power is in arbitrary units. Note that although the scintillation power is clear at low frequencies, bias subtraction is relatively simple, and in this case a constant bias (dashed line) would be a good approximation over the range of frequencies covered by the fringe peak.

rotation with respect to the baseline orientation then gives a factor $\gamma_1 = \cos(2\phi)$. The mixing of linear with circular polarisation states due to phase changes on reflection gives a second factor γ_2 . If we define δ to be the phase shift between s and p polarisations at the siderostat mirror (itself a function of the angle of incidence of the starlight), then γ_2 is given by:

$$\gamma_2 = \cos^2(\delta/2) + \sin^2(\delta/2) \cos(4\phi) \quad (3)$$

For example, δ is 37 degrees for SUSI's siderostats at 900 nm and an angle of incidence of 45 degrees, which gives $\gamma = 0.991$ for the maximum ϕ of 6 degrees for dual-polarisation measurements RR Sco. Taking all of these effects into account, we estimate that for no observation will the true values for V_\parallel^2/V_\perp^2 be more than 0.6% higher than the measured values given in Table 2. This is smaller than statistical measurement errors.

3 RESULTS AND MODEL FITTING

As a first step in interpretation of the results, from the observed quantities in Table 2 we derive the quantities $V_\parallel - V_\perp$ and V_\perp . For R Car, we have averaged data into four points at projected baselines of 4.2 and 8.4 m and covering pulsational phases of ~ 0.08 and ~ 0.15 . Similarly, observations of RR Sco have been distilled into measurements at baselines of 5.0 and 10.0 m with a phase of 0.95. As the signal-to-noise of the initial observations is high, the transformation from the observed quantities in V^2 to $V_\parallel - V_\perp$ and V_\perp could be performed while preserving the symmetric Gaussian error distributions reasonably well.

We assume that thermal photons from the star can be well represented by a Uniform Disk (UD) visibility curve, and that the dust distribution is spherically symmetric. The first assumption that the star is UD-like is reasonable because at phases near maximum, the atmosphere of a Mira variable is expected to be relatively compact (e.g. see Ireland et al. (2004a)), and the filter was chosen so that there was minimal contamination by the TiO molecule. The second assumption that the dust is spherically symmetric is reasonable for R Car because of its low total polarisation. Although any measured polarisation may be interstellar, a low total polarisation

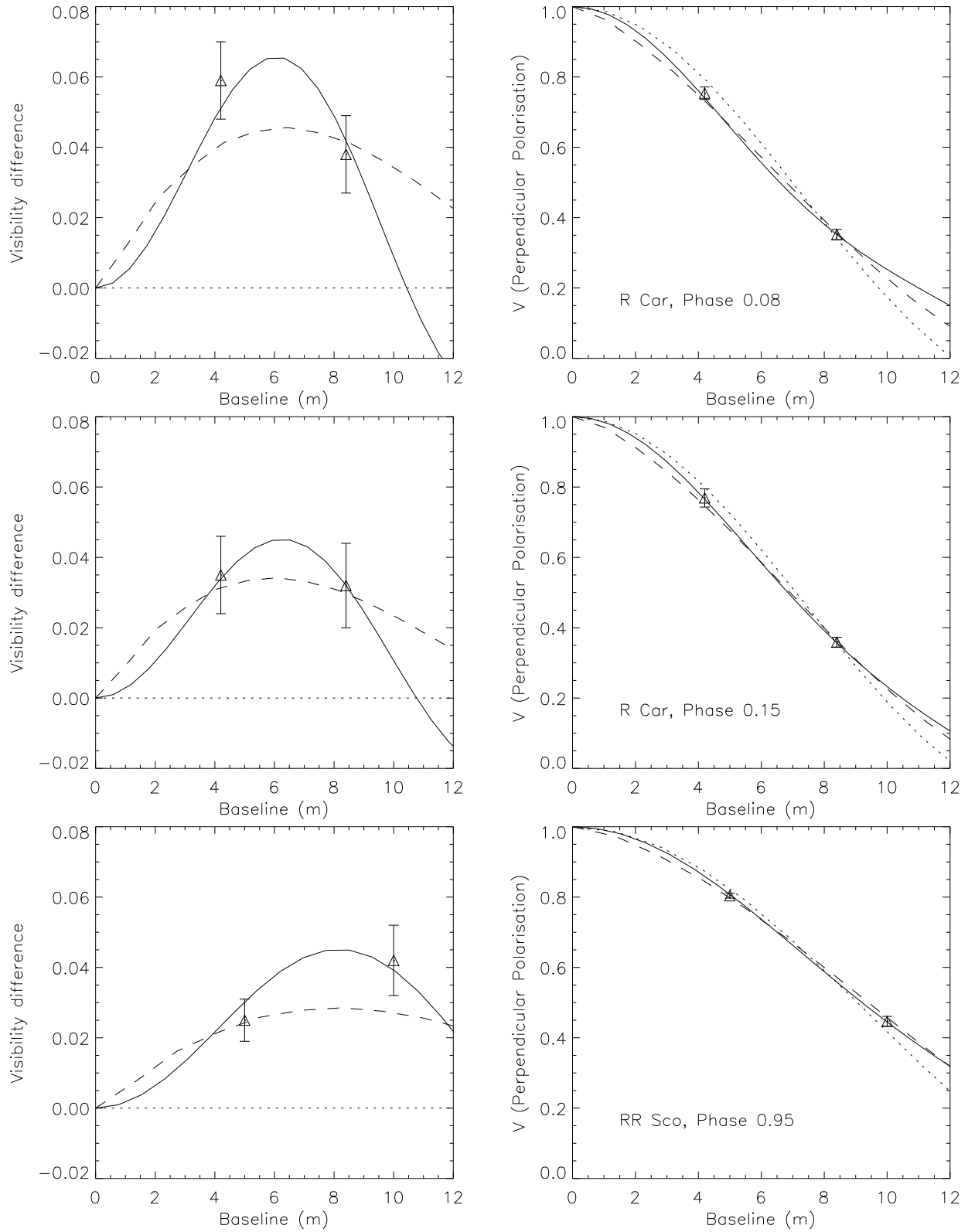


Figure 2. Fits to the first epoch (phase 0.08) of R Car (upper plots), the second epoch (phase 0.15) of R Car (middle plots) and the single epoch (phase 0.95) of RR Sco (lower plots) with data reduced to $V_{\parallel} - V_{\perp}$ (left plots) and V_{\perp} (right plots). The solid line is the thin shell model fit, the dashed line is the outflow model fit and the dotted line is the uniform disk only fit.

Table 2. Summary of SUSI observations of R Car and RR Sco. Visual phase (Col 4) were obtained from AAVSO data. The projected baseline B_p and position angle range are given in Cols 5 & 6, while the type of measurement and its recorded value are in Cols 7 & 8

Date	Star	JD	Phase	B_p (m)	PA range (°)	Measurement	Value
2004 Apr 8	R Car	2453104	0.08	4.2	-15..-6	V_{\perp}^2	0.582 ± 0.04
2004 Apr 8	R Car	2453104	0.08	8.4	1..18	V_{\perp}^2	0.123 ± 0.015
2004 Apr 8	R Car	2453104	0.08	4.2	-5..0	$V_{\parallel}^2/V_{\perp}^2$	1.160 ± 0.03
2004 Apr 9	R Car	2453105	0.08	4.2	-10..-2	V_{\perp}^2	0.556 ± 0.04
2004 Apr 9	R Car	2453105	0.08	8.4	5..10	V_{\perp}^2	0.125 ± 0.015
2004 Apr 9	R Car	2453105	0.08	8.4	-1..4	$V_{\parallel}^2/V_{\perp}^2$	1.220 ± 0.06
2004 May 1	R Car	2453127	0.15	4.2	-12..0	V_{\perp}^2	0.592 ± 0.04
2004 May 1	R Car	2453127	0.15	4.2	3..8	$V_{\parallel}^2/V_{\perp}^2$	1.095 ± 0.03
2004 May 2	R Car	2453128	0.15	8.4	-4..0	V_{\perp}^2	0.129 ± 0.01
2004 May 2	R Car	2453128	0.15	8.4	-4..-1	$V_{\parallel}^2/V_{\perp}^2$	1.150 ± 0.11
2004 May 6	R Car	2453132	0.16	8.4	0..5	$V_{\parallel}^2/V_{\perp}^2$	1.220 ± 0.10
2004 Jul 28	RR Sco	2453215	0.95	10.0	4..7	V_{\perp}^2	0.196 ± 0.012
2004 Jul 28	RR Sco	2453215	0.95	10.0	-10..-7	V_{\parallel}^2	0.259 ± 0.015
2004 Jul 28	RR Sco	2453215	0.95	10.0	-5..2	$V_{\parallel}^2/V_{\perp}^2$	1.195 ± 0.05
2004 Jul 29	RR Sco	2453215	0.95	5.0	-11..10	V_{\perp}^2	0.646 ± 0.01
2004 Jul 29	RR Sco	2453215	0.95	5.0	-2..5	$V_{\parallel}^2/V_{\perp}^2$	1.063 ± 0.014

signal places a rough upper-limit on the amount of light scattered by asymmetrical regions closest to the star. Measured polarisation fractions are 0.62% at 652 nm (McLean & Clarke 1977), 0.52% at 652.5 nm (Codina-Landaberry & Magalhaes 1980) and 0.51% in V band (Serkowski & Shawl 2001), with all authors measuring a significant downward trend in polarised fraction with increasing wavelength. These numbers can be compared with the roughly 15% total scattered light as measured in this paper at 900 nm. No such comprehensive polarimetry measurements could be found in the literature for RR Sco.

Two dust models were fit to the data: a thin shell and an outflow. For the thin shell model dust is assumed to exist in a static infinitesimally thin shell, while for the outflow model dust forms at some condensation radius and is then radiatively accelerated producing a stellar wind. For the outflow model, the dust density as a function of radius can be derived as (Schutte & Tielens 1989):

$$\rho(r) \propto 1/[(r - (1 - v_c^2))^{1/2} r^{3/2}] \quad (4)$$

Here r is radius in units of the condensation radius and v_c is the outflow velocity at r_c as a fraction of the final outflow velocity. We only consider the limiting case of $v_c = 0$ in this paper as it provides a better fit to the data in all cases. After fixing v_c to zero, both models have only two free parameters, the radius of dust formation and the optical depth of the dust shell. In both models, we assume that the dust grain radii are much smaller than the observing wavelength, so that the Rayleigh scattering approximation can be used, and the light scattered by the dust is all assumed to originate from the central star (i.e. only a single scattering is included).

The polarisation signal from a dust shell illuminated by an extended photosphere will be weaker than that illuminated by a compact object (or point source) of equivalent luminosity at the stellar centre. We proceed here to derive the dilution of the signal due to the geometrical extension of the underlying star. Consider a dust grain at a distance r_d from the centre of a star whose radius is r_s . The polarisation properties of light scattered from this grain will vary according to the angle of the incident photon, which in turn depends on the original location of the emission on the surface of the star. The net polarisation is then found by integration over the disk of the star visible to the dust grain.

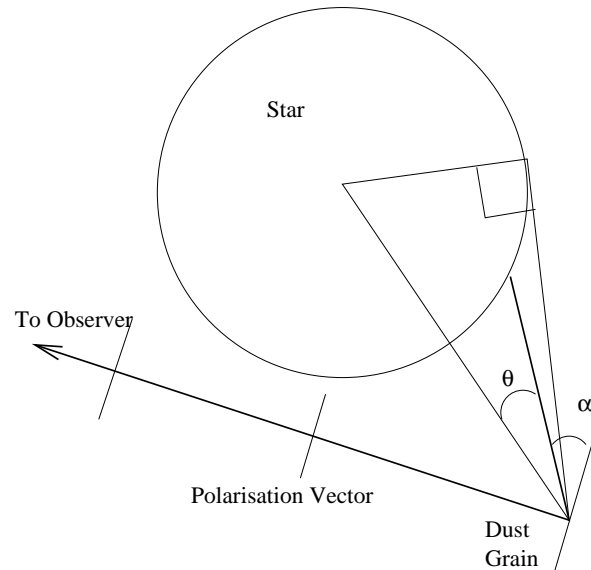


Figure 3. An example of the geometry for which the polarised intensity was calculated, using the approximation of Rayleigh scattering from an optically thin shell (see text).

For Rayleigh scattering, if the angle between the polarisation vector of the radiation seen by the observer and the ray incident on the dust grain is α , then the intensity of the scattered radiation is proportional to $\sin^2 \alpha$. Let θ be the angle between the ray incident on the dust grain and the direction from the dust grain to the star's centre, let ϕ be an azimuthal coordinate describing a ring on the stellar surface and let β be the angle between the vector from the star's centre to the dust grain and the vector from the dust grain to the observer. An example of this geometry when all vectors are coplanar is shown in Figure 3. Then, using spherical trigonometry, α can be expressed in terms of θ , ϕ , and β . The integral that gives the scattered intensity is:

$$I = \int_0^{2\pi} d\phi \int_0^{\arcsin \frac{r_s}{r_d}} \sin \theta \sin^2 \alpha d\theta \quad (5)$$

We consider the polarised intensities of scattered light from the dust grain decomposed into those with electric fields in radial (I_r) and azimuthal (I_a) directions with respect to the centre of the underlying disk. Evaluating the integral for I_r and I_a gives:

$$I_r = \frac{2-u-u^2}{3} + \frac{u+u^2}{2} \cos^2 \beta \quad (6)$$

$$I_a = \frac{4+u+u^2}{6} \quad (7)$$

$$\text{where } u = \sqrt{1 - \frac{r_s^2}{r_d^2}} \quad (8)$$

These integrals are normalised so that forward scattering from a point source gives intensities of 1. Note that for dust distant from the star, $u = 1$ and this formula reduces to the familiar formula for Rayleigh scattering. These intensities were numerically integrated for the two distributions of dust discussed above to give a two-dimensional image, and a two-dimensional Fourier transform applied to this image to give the visibility functions arising from the dust scattering. Radiation back-scattered onto the surface of the star was assumed to be absorbed. After normalising these dust visibility functions to 1 at zero baseline, the overall visibility functions become:

$$V_{\parallel} = \frac{e^{-\tau_d} V_s + (1-x_b)(1-e^{-\tau_d}) V_{d\parallel}}{1-x_b(1-e^{-\tau_d})} \quad (9)$$

$$V_{\perp} = \frac{e^{-\tau_d} V_s + (1-x_b)(1-e^{-\tau_d}) V_{d\perp}}{1-x_b(1-e^{-\tau_d})} \quad (10)$$

Here τ_d is the optical-depth of the dust, $V_{d\perp}$, $V_{d\parallel}$ and V_s are the visibility functions for the dust in both polarisations and the star respectively, and x_b is the fraction of the scattered light backscattered to re-intercept the surface of the star. The derived fit parameters for both stars are given in Table 3, with the fits for both stars shown graphically in Figure 2. In addition to quantities derived from fitting to the high-resolution data, for comparison in Table 3 we also present expected stellar diameters based on the observed luminosities. These are given in the Model D_s column, and were derived using near-maximum dust-free M series atmospheric models from Ireland et al. (2004a) (interpolating between the M08, M09n and M10 models), with the distance of the model star set to match the K band magnitudes measured by Whitelock et al. (2000) at the same phases. Note that the J-K colours of these stars as measured by Whitelock et al. (2000) are consistent with this model series within the observational cycle-to-cycle scatter.

4 DISCUSSION

The dust free (UD only) fits in Table 3 are clearly eliminated for both stars. The high χ^2 values have their origin in the inability of this scattering-free model to generate any polarisation signal. Of the two models with dust, the thin shell model is a better fit than the outflow model for both stars. The best-fit condensation radii in the outflow models are also uncomfortably close to the continuum-forming photospheres for both stars. Although there may be dust types that could plausibly exist in thermal equilibrium with the radiation field at these radii (as discussed below), the gas temperatures in the model star of Section 1 are 2000 K at 1.1 stellar radii, much too high for grain nucleation (e.g. see the discussion in Jeong et al. (2003)). The only way dust could exist so close to the continuum-forming photosphere is if it had formed at near-minimum phases

and then fallen in. However, this kind of motion is in conflict with the general assumptions of the outflow model.

The two epochs of R Car do not show statistically significant differences, but the small differences at the level of about $1-\sigma$ are in the expected direction. The star appears to increase in apparent size from phase 0.08 to 0.15, as predicted by the models, and the optical-depth in scattering appears to decrease, consistent with the dust being part of an infalling layer that is partially sublimating at these near-maximum phases. For RR Sco, the discrepancy between the luminosity/model-predicted diameter and the best fit diameter is almost certainly due to contamination from the TiO molecule. A moderate strength TiO band at 850 nm is included in the wing of the SUSI filter profile which could account for the enlargement observed, although predicting the effects of such molecular contamination is made difficult by its strongly cycle-dependent nature (Ireland et al. 2004a).

From the discussion of dust formation radii in Section 1, it is clear that “dirty” silicates cannot form a major fraction of the optical depth in scattering due to dust around R Car. For survival within the hostile environment close to the photosphere, dust must have very low absorption between 1 and 4 μm where most of the radiation from the central star is emitted, and higher absorption coefficients at longer wavelengths promoting efficient radiative cooling. Corundum is a clear possibility here, but another obvious dust type that satisfies these criteria is forsterite, the Mg-rich olivine that is predicted to be the first significant silicate to form in chemical equilibrium calculations (Gail & Sedlmayr 1999). The optical constants for this dust species as given in Jäger et al. (2003) result in absorption coefficients 300 times higher at 10 μm than at 2 μm . This dust is stable at a radius of 1.2 stellar radii from the 3000 K model star of Section 1. As a plausible and abundant dust candidate, we will assume that the dust around these stars is made of forsterite for the following analysis of the implications of the dust model parameters.

Low absorption at wavelengths where the bulk of the stellar radiation is emitted also results in lower radiation pressure on the dust. Assuming full dynamical coupling between the gas and dust and full Mg condensation, we can calculate the radiative acceleration as a fraction of the gravitational acceleration for an optically-thin model dust shell. For a shell made of forsterite around the 3000 K model star of Section 1 using Mie theory to calculate absorption and scattering coefficients, this fraction is 41% for spherical grains of radius 0.1 μm and 1.5% for grains of radius 0.02 μm . We therefore propose that this dust is formed in material primarily elevated by shocks, which in turn means that significant temporal variation in the dust shell optical depth and/or radius is expected.

Where the Rayleigh limit of small particles with respect to the wavelength of scattered light applies, it is sufficient to approximate dust with a distribution of sizes as a homogeneous population with a single effective radius a_e . For dust composed of forsterite, with a scattering optical depth of 0.15 at 900 nm, typical of the observations presented here, the optical depth in absorption at 10 μm is 1 for $a_e = 55 \text{ nm}$. Results from a radiative transfer model of a geometrically thin shell of forsterite with a fixed temperature of 1100 K and an optical-depth of 1 at two stellar radii from the centre of a spherical black-body 3000 K star are displayed in Figure 4. It can be seen that there is no strong mid-infrared feature evident in either emission or absorption due to the dust shell. It would seem that the dust here represents an intermediate case between the compact geometries typically yielding absorption features, and spectra exhibiting emission which is usually associated with extended geometries. This result was found to be robust, and insensitive to the

Table 3. Fit parameters for both epochs of R Car and the single epoch of RR Sco, giving the apparent stellar diameter D_s , a model value for D_s (see text), the diameter of the dust condensation shell D_c the optical depth at 900 nm τ_{900} and the reduced χ^2 for the fit. Note that there is only one degree of freedom for the Thin Shell and Outflow models. Details of models given in the text.

Star	Phase	Fit Type	D_s (mas)	Model D_s (mas)	D_c (mas)	τ_{900}	χ^2
R Car	0.08	Thin Shell	15.8 ± 0.6	14.9	32.3 ± 1.9	0.19 ± 0.03	1.2
R Car	0.08	Outflow	15.6 ± 0.6	14.9	17.3 ± 3.1	0.38 ± 0.07	4.5
R Car	0.08	UD Only	18.7 ± 0.3	14.9	-	-	15.4
R Car	0.15	Thin Shell	16.6 ± 0.6	16.0	31.3 ± 3.6	0.14 ± 0.04	0.1
R Car	0.15	Outflow	16.2 ± 0.6	16.0	18.3 ± 3.8	0.26 ± 0.06	0.9
R Car	0.15	UD Only	18.4 ± 0.3	16.0	-	-	6.3
RR Sco	0.95	Thin Shell	12.3 ± 0.4	8.3	24.0 ± 2.0	0.14 ± 0.03	1.1
RR Sco	0.95	Outflow	12.3 ± 0.4	8.3	13.5 ± 2.2	0.22 ± 0.04	3.7
RR Sco	0.95	UD Only	14.5 ± 0.2	8.3	-	-	16

optical-depth of the shell. Note, however, that a shell of forsterite with a 10 micron optical-depth much greater than 1 would heat up beyond its sublimation temperature at the inner edge of the thin dust shell. In order to meet this criteria while maintaining the observed 900 nm optical depth, the effective particle size a_e is constrained to be larger than about 50 nm. From the point of view of energetics, the failure of the dust to have a profound impact on the spectrum is simply a consequence of its optical properties: its inability to absorb in the near-infrared means that it cannot redistribute the bulk of the stellar flux. The dust scattering measured by the technique in this paper is thus largely independent of the form of the infrared spectrum, and could therefore have remained hidden from investigations based on SED fitting. By this argument, the mid-infrared excess in the spectrum must come from a material that absorbs more strongly than forsterite in the near-infrared. Dust that has evolved and been enriched with iron (that condenses at lower temperatures) in an outflow consisting of shells partially ejected in previous pulsation cycles could satisfy this property. More detailed mid-infrared spectral modeling is beyond the scope of this paper, but would need to include the emission from the extended molecular atmosphere as predicted by self-consistent modeling by Jacob & Scholz (2002) and semi-empirical modeling of Weiner (2004) and Ohnaka (2004).

The dust uncovered here is not inconsistent with the mid-infrared measurements of Danchi et al. (1994). These authors fit an outflow model to R Leo (which has slightly more pronounced mid-infrared emission than either R Car or RR Sco), with an optical depth at $11\mu\text{m}$ of 0.1. For forsterite dust with $a_e = 55\text{ nm}$, this corresponds to a 900 nm optical depth of 0.025. If a similar outflow were to exist around RR Sco or R Car in addition to the shell model, then its effect on the fit parameters in Table 3 would be roughly within the quoted errors. In order to measure scattering from such an outflow, shorter baselines and higher precision would be required.

Both R Car and RR Sco have relatively low mass-loss rates as constrained by CO line observations. Groenewegen et al. (1999) modeled the mass loss rate for RR Sco to be $1.1 \times 10^{-8} M_\odot$ per year and that of R Car to be less than $1.6 \times 10^{-9} M_\odot$ per year. If we assume full Mg condensation at solar metallicity, then our best fit model with a shell at 2 stellar radii and an optical-depth 0.15 in scattering at 900 nm has a total mass of $2.8 \times 10^{-6} M_\odot$ if we continue our assumptions of dust composed of forsterite with $a_e = 0.55\text{ nm}$ and full condensation. Less than full condensation, or dust composed of the lower-abundance corundum would give an even higher mass shell. This means that the observed mass-loss

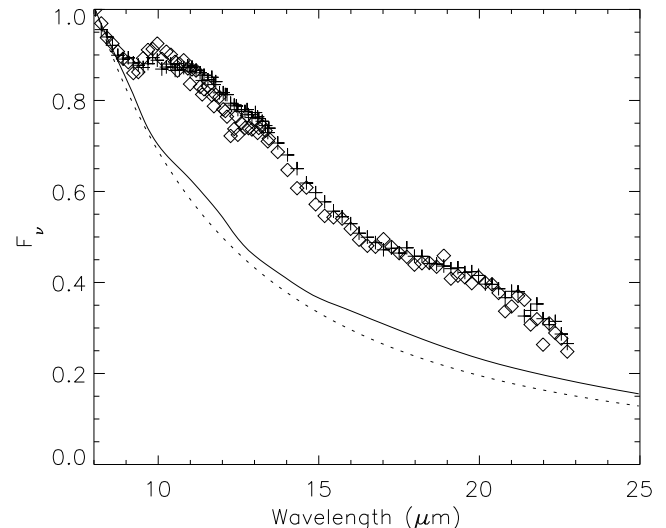


Figure 4. An example mid-IR spectrum (solid line) for a 1100 K thin-shell model with a $10\mu\text{m}$ optical-depth of 1 at 2 stellar radii, illuminated by a star with a 3000 K black-body spectrum. Flux is normalised to the $8\mu\text{m}$ flux, and the 3000 K black-body spectrum is overlaid for reference (dotted line). Normalised IRAS Low Resolution Spectrometer (LRS) spectra are overplotted for R Car (crosses) and RR Sco (diamonds). The emission features in these spectra almost certainly come from a region geometrically more distant than that probed here (see text).

rates are only consistent with the thin-shell model as long as the shell is considered nearly static, taking hundreds or thousands of pulsational cycles for material in the shell to be fully ejected. This is in turn consistent with the low radiative acceleration expected from dust that can exist so close to the stars.

Outflow models, on the other hand, were not so easy to fit within a self-consistent picture of stellar mass loss. Using the measured CO outflow velocity from Young (1995) of 3 km/s for RR Sco we can calculate the mass-loss rate from a typical outflow model in Table 3. Again assuming full Mg condensation at solar metallicity for forsterite dust with $a_e = 55\text{ nm}$, the mass loss rate for a model with our best fit optical-depth 0.25 in scattering at 900 nm and condensation radius of 1.1 stellar radii is $2.7 \times 10^{-7} M_\odot$ per year, much higher than the observed mass-loss rates. This demonstrates once again that the outflow model can be ruled out.

5 CONCLUSION

Using optical interferometric polarimetry, we have spatially separated the component of flux at 900 nm scattered by dust around the Mira variables R Car and RR Sco from their photospheric emission. We found that the inner radius of dust formation around these stars to be less than three stellar radii, consistent with dust that is relatively transparent between 1 and 4 μm , such as iron-poor silicates or corundum. This dust exists in a shell-like structure around these stars that may have little influence on their mid-infrared spectra and is not part of an outflow. This result demonstrates the complexity of the circumstellar environment of Mira variables where mass loss and dust formation are only made possible by pulsation. Simple outflow models are grossly inadequate, and it is necessary to consider the changing optical properties of dust as it evolves from the condensation radius outwards.

ACKNOWLEDGMENTS

Visual data for estimating the variability phases of targets at the times of the SUSI observations were obtained from the AAVSO website. We thank M. Scholz for many valuable discussions, and all the SUSI group members for their help in supporting the instrument. This research was supported by the Australian Research Council and the Deutsche Forschungsgemeinschaft within the linkage project “Red Giants.”

REFERENCES

Baldwin J. E., Boysen R. C., Cox G. C., Haniff C. A., Rogers J., Warner P. J., Wilson D. M., Mackay C. D., 1994, in Proc. SPIE Vol. 2200, p. 118-128, Amplitude and Intensity Spatial Interferometry II, James B. Breckinridge; Ed. Design and performance of COAST. pp 118–128

Brown R. H., Davis J., Allen L. R., 1974, MNRAS, 168, 93

Claret A., 2000, A&A, 363, 1081

Codina-Landaberry S. J., Magalhaes A. M., 1980, AJ, 85, 875

Cohen M., Walker R. G., Carter B., Hammersley P., Kidger M., Noguchi K., 1999, AJ, 117, 1864

Danchi W. C., Bester M., Degiacomi C. G., Greenhill L. J., Townes C. H., 1994, AJ, 107, 1469

Davis J., Ireland M., North J., Tango W., Tuthill P., 2005, MNRAS, (In Preparation)

Davis J., Tango W. J., Booth A. J., Thorvaldson E. D., Giovannis J., 1999, MNRAS, 303, 783

Dorschner J., Begemann B., Henning T., Jaeger C., Mutschke H., 1995, A&A, 300, 503

Ducati J. R., 2002, VizieR Online Data Catalog, 2237, 0

Egan M. P., Sloan G. C., 2001, ApJ, 558, 165

Elias N. M., 2004, ApJ, 611, 1175

Gail H.-P., Sedlmayr E., 1999, A&A, 347, 594

Groenewegen M. A. T., Baas F., Blommaert J. A. D. L., Stehle R., Josselin E., Tilanus R. P. J., 1999, A&AS, 140, 197

Habing H. J., 1996, A&A Rev., 7, 97

Ireland M. J., Scholz M., Tuthill P. G., Wood P. R., 2004a, MNRAS, 355, 444

Ireland M. J., Tuthill P. G., Bedding T. R., Robertson J. G., Jacob A. P., 2004b, MNRAS, 350, 365

Jäger C., Dorschner J., Mutschke H., Posch T., Henning T., 2003, A&A, 408, 193

Jacob A. P., Scholz M., 2002, MNRAS, 336, 1377

Jeong K. S., Winters J. M., Le Bertre T., Sedlmayr E., 2003, A&A, 407, 191

Jones T. W., Merrill K. M., 1976, ApJ, 209, 509

Kervella P., Fouqué P., Storm J., Gieren W. P., Bersier D., Mourard D., Nardetto N., Foresto V. C. d., 2004, ApJ, 604, L113

Koike C., Kaito C., Yamamoto T., Shibai H., Kimura S., Suto H., 1995, Icarus, 114, 203

McLean I. S., Clarke D., 1977, MNRAS, 179, 293

Ochsenbein F., Halbwachs J. L., 1982, A&AS, 47, 523

Ohnaka K., 2004, A&A, 424, 1011

Ossenkopf V., Henning T., Mathis J. S., 1992, A&A, 261, 567

Salpeter E. E., 1977, ARA&A, 15, 267

Schutte W. A., Tielens A. G. G. M., 1989, ApJ, 343, 369

Serkowski K., Shawl S. J., 2001, AJ, 122, 2017

van Belle G. T., 1999, PASP, 111, 1515

Weiner J., 2004, ApJ, 611, L37

Whitelock P., Marang F., Feast M., 2000, MNRAS, 319, 728

Young K., 1995, ApJ, 445, 872